Magnetic Circular Dichroism of the Hydroxyl Radical in an Argon Matrix

Vaughan S. Langford and Bryce E. Williamson*

Department of Chemistry, University of Canterbury, Private Bag 4800, Christchurch, New Zealand

Received: January 6, 1997; In Final Form: February 21, 1997[⊗]

Magnetic circular dichroism (MCD) and absorption spectra are reported over the temperature range 1.7−7 K and the magnetic field range 0−4 T for the hydroxyl free radical isolated in an Ar matrix (OH/Ar). The data indicate a reduction of the orbital angular momentum of the lowest electronic level of the guest. This is interpreted within the framework of a crystal field model involving the Ar atoms of the host lattice. The conclusions are that the OH guest radicals are randomly oriented, occupy at least five distinct sites, and have orbital reduction factors in the range $\kappa = 1.00$ to 0.54.

I. Introduction

The free radical OH (hydroxyl) occurs in a broad range of environments and is an important species in a large range of chemical processes. It is observed in extraterrestrial systems, including the interstellar medium,[1] cometary outflows,[2] and the atmospheres of stars.[3] In terrestrial environments, it appears as an intermediate in combustion reactions[4] and is involved in atmospheric chemistry,[5] being the dominant oxidant in the troposphere. It is an important contributor to the catalytic destruction of ozone (responsible for approximately 20% of the natural ozone loss) and undergoes many other reactions, down to sea level. It has even been found to play a (generally destructive) role in biological processes.[6,7]

For many years gas-phase $A^2\Sigma^+ \rightarrow X^2\Pi$ emission of OH ($\lambda_{0,0} \approx 308$ nm) was observed in Giesler tubes containing water vapor, but it was not until 1924 that Watson attributed the spectrum to OH.[8] In 1927, Mulliken published a detailed theoretical interpretation of the spectra of a number of diatomic molecules, including OH.[9] The experimental work was later extended by Johnston and co-workers[10−12] using improved experimental apparatus and longer photographic exposure times. Since then, there has been a large number of investigations of gas-phase OH and (to a lesser extent) OD.[13]

OH was first isolated in an Ar matrix (OH/Ar) by Robinson and McCarty,[14] by creating a discharge through Ar and moist hydrazine and depositing the resultant mixture onto a liquid He cooled sample window. The (0,0) absorption band of the $A^2\Sigma^+ \leftarrow X^2\Pi$ transition was found to by red-shifted by $\sim$300 cm^{-1} relative to the gas phase. Subsequently, they measured electronic absorption spectra of OH[15,16] and OD[16] in Ar and Kr matrixes, reporting fine structure that was very similar for both hosts and which changed only slightly between OH and OD. The relative invariance to isotopic substitution suggests that the structure is not a consequence of rotational dynamics. Wei corroborated McCarty and Robinson's results and also found that the spectra OH and OD in Xe show similar structure.[17] However, spectra of OH/Ne and OD/Ne showed significantly different, isotope-dependent structure, which was interpreted in terms of perturbed rotational dynamics and translation−rotation coupling.[18,19]

In 1986, Rose reported magnetic circular dichroism (MCD) and absorption spectra of OH/Ar.[20] The spectral resolution was inadequate for structure to be observed, but she found that the magnitude of the MCD increased between the (nominal) temperatures of $\sim$8 and 3 K. Earlier ESR spectra of OH in γ-irradiated ice had shown the ground-state orbital angular momentum to be totally quenched,[21−24] but the observation of MCD temperature dependence requires that quenching is incomplete in the case of OH/Ar. Unfortunately, MCD calibration and thermometry problems prevented her from obtaining a reliable measure of the degree of orbital reduction.

In this paper, MCD and absorption spectra are reported for OH/Ar at accurately determined temperatures between 7 and 1.7 K and at magnetic fields up to 4 T. The aims of this work are (i) to provide a quantitative measure of the ground-state orbital angular momentum and hence the orbital reduction factor and (ii) to determine the origins of the structure observed in the absorption spectra.

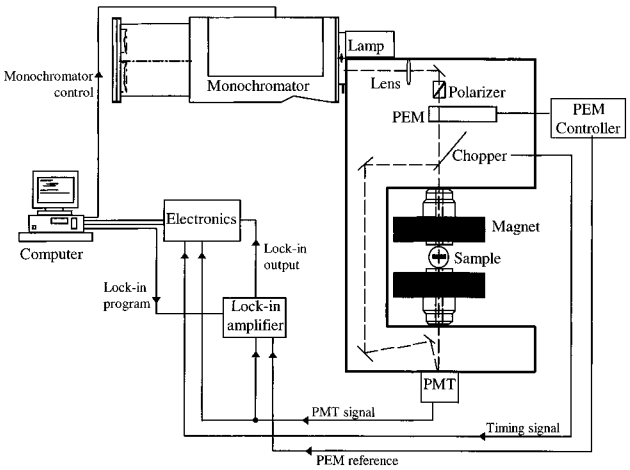

Figure 1. Schematic diagram of the spectrometer used for simultaneous measurement of magnetic circular dichroism and double-beam absorption spectra. For high-field and low-temperature measurements, the electromagnet shown here is replaced by a superconducting magneto-cryostat. See section II for further description.

II. Experimental Section

MCD and double-beam absorption spectra were measured simultaneously using the spectrometer illustrated in Figure 1. Light from a 300-W Xe arc lamp (ILC Technology LX300UV) is dispersed by a 1-m Czerny-Turner monochromator (Jarrell-Ash 78-463 with a 300-nm blaze grating), collimated, and then circularly polarized by the combined action of a Glan-Taylor prism and a photoelastic modulator (Hinds International PEM-IF4) operating at $\sim$50 kHz. A mirrored chopper (11 Hz) passes

* Corresponding author. E-mail: B.Williamson@chem.canterbury.ac.nz. Fax: ++64 3 364 2110.

[⊗] Abstract published in *Advance ACS Abstracts,* April 1, 1997.

S1089-5639(97)00076-5 CCC: $14.00

TABLE 1: Parameters for the $A^2\Sigma^+ \leftarrow X^2\Pi$ Bands of OH/Ar

band[a]	E/cm^{-1} [b]	$\mathbf{A}_0(i)/\mathbf{A}_0$[c]	κ	V/cm^{-1}	$g_{\|\|}{}^-$	$g_\perp$
1	32 025	0.08	1.00	0	4.0	0.0
2	32 095 (32 090)	0.29	0.91	56	3.8	0.8
3	32 165 (32 155)	0.35	0.77	103	3.5	1.3
4	32 230 (32 225)	0.19	0.54	194	3.1	1.7
5	32 285	0.09	0.55	189	3.1	1.7
overall[d]	32 170 (~32 155)	1.00	0.79 ± 0.02	97 ± 10	3.58 ± 0.04	1.23 ± 0.05

[a] Numbering for cross reference with Figures 2 and 7. [b] Band barycenters ± 10 cm^{-1}. Values in parentheses are from ref 15. [c] Zeroth absorption moments, expressed as a fraction of the total $\mathbf{A}_0$, obtained by least-squares fitting of the OH/Ar absorption spectrum in Figure 2 using Gaussian bands. [d] Obtained from a least-squares fit of eq 30 to the data in Figure 4, assuming random molecular orientation and $\zeta_\pi = 125 \pm 10$ cm^{-1}.

light alternately through a sample in the axial bore of a magnet (either Alpha Magnetics 4800 0.7-T electromagnet or Oxford Instruments SM4 6-T superconducting cryomagnet) and through the reference path to a Hamamatsu R-292 photomultiplier tube (PMT). The chopper also provides a short "dark" period and produces a timing signal that is used to synchronize data acquisition.

Spectrometer control, data acquisition, and digital signal processing are achieved by using an IBM-compatible 486-SX computer equipped with an Advantech PCL-814B interface card. Electronic sampling gates, corresponding to the "sample", "reference" and "dark" periods, are generated from the chopper timing signal. The dc levels measured during these periods are used to calculate the double-beam absorption, signal averaging being achieved by multiple analogue-to-digital conversions during each period. The 50-kHz ac signal component is measured continuously by a programmable lock-in amplifier (Stanford Research Systems SR510) referenced to the PEM frequency. The analogue output of the SR510 is electronically integrated by external electronics over the "sample" period, then read by computer, and used to calculate the MCD.

Preliminary experiments were performed by using a closed-cycle He refrigerator (APD Cryogenics) placed between the poles of the electromagnet. These allowed the determination of optimum deposition and annealing conditions, concentrations, and spectrometric parameters for later runs using the SM4 cryomagnet. Purified H_2O or D_2O vapor was mixed in a 1:100 mole ratio with Ar in a 1-L gas reservoir to give a total pressure of ~1 atm. The mixture was allowed to flow through a 4-mm (i.d.) glass tube at a rate of ~6 mmol h^{-1}, while being subjected to Ar-resonance radiation produced by a Tesla-coil discharge. The products were deposited onto a cryogenically cooled c-cut sapphire sample window held at ~15 K. Deposition times were ~15 min. Annealing resulted in slightly sharper bands; however, it did not significantly change the structure and had the detrimental effects of reducing the OH (or OD) concentration and clouding the matrixes. For the data reported below, the matrixes were not annealed.

The final experiments for OH/Ar employed the SM4 cryomagnet in a matrix-injection mode that is described elsewhere.[25] Temperatures above 4.2 K were obtained by operating the SM4 sample chamber as continuous-flow cryostat, using cold He vapor as the exchange gas and monitoring the temperature with a carbon resistance thermometer. Temperatures below 4.2 K where achieved by filling the sample chamber with liquid He and then reducing the vapor pressure over the liquid by using a rotary vane pump and Oxford Instruments MNT manostat. The vapor pressure (measured by a MKS Baratron 1000-Torr capacitance manometer) was used to determine the temperature of the cryogenic fluid in which the sample was immersed.

Spectra were obtained using a spectral resolution of ~0.16 nm. Depolarization of circularly polarized light by the matrix was checked by measuring the natural circular dichroism of a solution of Λ-tris(1,2-ethanediamine)cobalt(III) placed between the sample and PMT and found to be negligible.

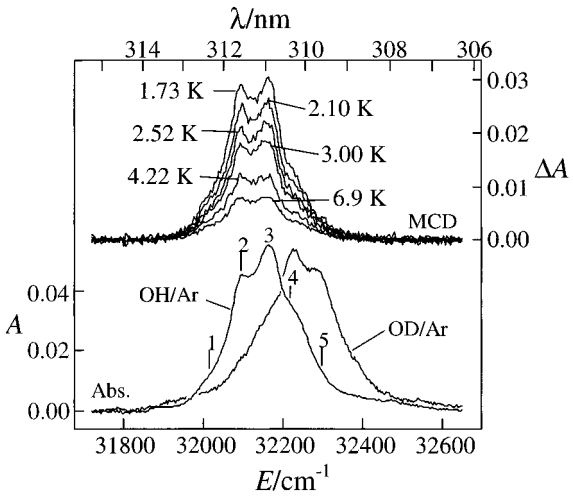

Figure 2. Top: MCD (ΔA) of OH/Ar between 1.73 and 6.9 K. Bottom: absorption spectra (A) of OH/Ar and OD/Ar. The absorption bands of OH/Ar are labeled for cross reference with Table 1 and Figure 7.

III. Results

Figure 2 shows the (temperature-independent) absorption spectra of OH/Ar and OD/Ar and the temperature dependence of the MCD of OH/Ar (at a field of 1 T) between 1.73 and 6.9 K. Each spectrum exhibits a pair of maxima and a number of shoulders spaced at roughly regular intervals. The barycenters for the OH/Ar bands (labeled 1−5 in Figure 2) are given in Table 1. The three strongest bands (2−4) were observed by McCarty and Robinson[15] at the positions indicated in parentheses in Table 1.

The spectrum of OD/Ar was obtained at ~12 K using the refrigerator/electromagnet system. It has a general appearance similar to that of OH/Ar but is blue-shifted by ~1 nm and shows a different distribution of intensity between the individual bands.

The MCD is single signed (positive) and shows the reciprocal temperature dependence that is characteristic of C terms and indicative of ground-state degeneracy.[26] The field dependence of the MCD, between 0 and 4 T, at $T = 1.73$ K, is illustrated in Figure 3. To quantify these dependencies, we define dimensionless zeroth moment parameters, which measure the area under the band:

$$\mathbf{A}_0 = \int \frac{A(E)}{E}\,\mathrm{d}E \tag{1}$$

$$\mathbf{M}_0 = \int \frac{\Delta A(E)}{E}\,\mathrm{d}E \tag{2}$$

where E is the energy of the incident radiation, A and ΔA are,

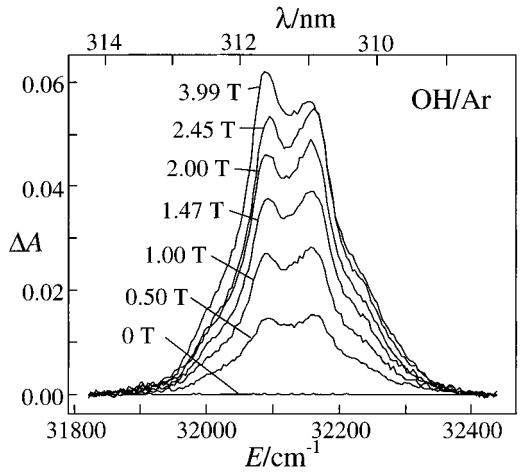

Figure 3. Magnetic-field dependence, between 0 and 4 T, of the MCD of OH/Ar at 1.73 K.

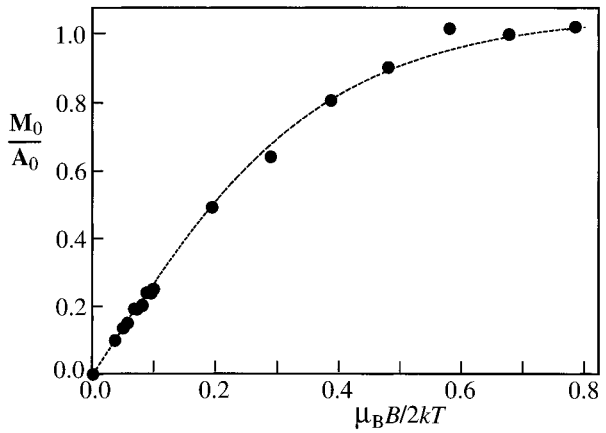

Figure 4. Magnetization saturation data for the moment ratio $\mathbf{M}_0/\mathbf{A}_0$ as a function of $\mu_B B/2kT$ for OH/Ar. The broken curve is the best fit to the data assuming random orientation of the guest radical and $\zeta_\pi = 125 \pm 10$ cm^{-1} and was obtained with an orbital reduction factor of $\kappa = 0.79 \pm 0.02$.

respectively, the absorbance and the MCD, and the integrals are carried over the full envelope of the transition. The ratios $\mathbf{M}_0/\mathbf{A}_0$ for the spectra in Figures 2 and 3 are plotted against $\mu_B B/2kT$ in Figure 4 (μ_B and k are, respectively, the Bohr magneton and Boltzmann's constant); these show the magnetic saturation behavior that is again typical of *C* terms.[26]

IV. Discussion

The transition responsible for the spectra of Figures 2 and 3 is $A^2\Sigma^+ \leftarrow X^2\Pi$, arising from the excitation $3\sigma^1 1\pi^4 \leftarrow 3\sigma^2 1\pi^3$. In the gas phase, $X^2\Pi$ is split by spin−orbit (SO) interactions (Figure 5) into levels quantized by the projection of the total electronic angular momentum along the internuclear (*z*) axis ($\Omega = {}^1/_2, {}^3/_2$). The SO states are designated $|^2\Pi_\Omega\ M_\Omega\rangle$ ($M_\Omega = \pm\Omega$) and have SO energies

$$E(^2\Pi_\Omega) = -\zeta_\pi \Lambda(\Omega - \Lambda) \tag{3}$$

Λ is the projection of the orbital angular momentum along *z* ($\Lambda = 1$ for a Π state) and ζ_π is an empirical SO coupling constant for a 1π electron. $\zeta_\pi = 139$ cm^{-1} in the gas phase,[13] and the inverted nature of the term ($E(^2\Pi_{3/2}) < E(^2\Pi_{1/2})$) is accounted for by the leading negative sign in eq 3.

When OH is incorporated into condensed media and exposed to a magnetic field, the electronic states are modified by crystal field (due to the presence of neighboring species) and Zeeman

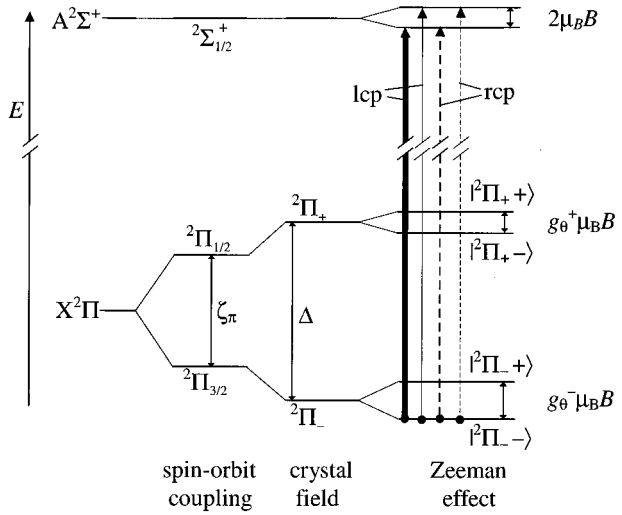

Figure 5. Energy-level diagram showing the effects of spin−orbit, crystal-field, and Zeeman interactions on the $X^2\Pi$ and $A^2\Sigma^+$ states of OH/Ar. Parameters and state designations are defined in section IV. The relative intensities of left- (lcp) and right-circularly polarized (rcp) transitions originating from the $|^2\Pi_-\rangle$ state and terminating in the $A^2\Sigma^+$ manifold are qualitatively indicated by the thickness of the lines.

interactions, the effects of which are reflected in the absorption and MCD spectra.

1. Crystal Field Effect. The $X^2\Pi$ term is susceptible to first-order crystal field (CF) effects that transform as part of the symmetric square of the orbital irrep; $[\Pi^2] = \Sigma^+ \oplus \Delta$. The totally symmetric (Σ^+) component shifts the levels but does not contribute to their splitting. On the other hand, the Δ component (which corresponds to an orthorhombic field) lowers the orbital degeneracy and mixes the SO states. If we designate the strength of the latter component by *V*, then the combined SO-CF splitting of the $X^2\Pi$ manifold (Figure 5) is

$$\Delta = (\zeta_\pi{}^2 + V^2)^{1/2} \tag{4}$$

where the value of ζ_π will be slightly reduced from the gas-phase values.[27,28] The SO-CF eigenstates are

$$|^2\Pi_+ \pm 1/2\rangle = \pm\beta\,|^2\Pi_{3/2} \pm 3/2\rangle + \alpha\,|^2\Pi_{1/2} \mp 1/2\rangle \tag{5a}$$

$$|^2\Pi_- \pm 1/2\rangle = \alpha\,|^2\Pi_{3/2} \pm 3/2\rangle \mp \beta\,|^2\Pi_{1/2} \mp 1/2\rangle \tag{5b}$$

where $^2\Pi_+$ and $^2\Pi_-$ respectively designate the upper and lower SO-CF levels, and $\pm 1/2$ on the left denote the values of M_S. The mixing coefficients are

$$\alpha = V/(V^2 + (\Delta - \zeta_\pi)^2)^{1/2} \tag{6}$$

$$\beta = (\Delta - \zeta_\pi)/(V^2 + (\Delta - \zeta_\pi)^2)^{1/2} \tag{7}$$

These coefficients obey the relations

$$\alpha^2 + \beta^2 = 1 \tag{8}$$

$$\alpha^2 - \beta^2 = \zeta_\pi/\Delta \equiv \kappa \tag{9}$$

$$2\alpha\beta = V/\Delta \equiv \eta \tag{10}$$

One of the consequences of the CF is a redistribution of electronic angular momentum. The relevant matrix elements are listed in Table 2, where the *g* values are

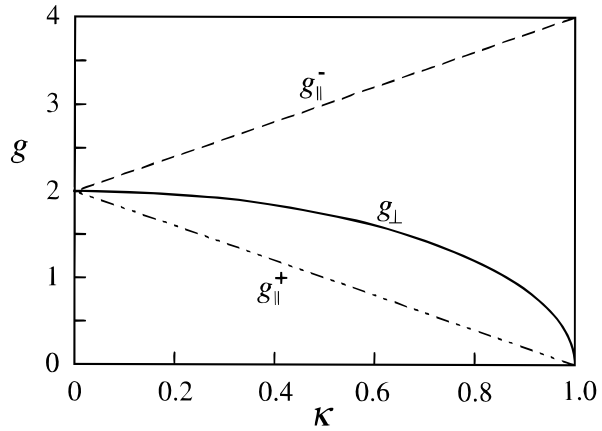

Figure 6. Dependence of g values for the $X^2\Pi$ term of OH/Ar on the orbital reduction factor, κ.

TABLE 2: Angular Momentum Matrix Elements for the $X^2\Pi$ SO-CF States of OH/Ar[a]

$L_z + 2S_z$	$\|^2\Pi_- -1/2\rangle$	$\|^2\Pi_- 1/2\rangle$	$\|^2\Pi_+ -1/2\rangle$	$\|^2\Pi_+ 1/2\rangle$
$\langle^2\Pi_- -1/2\|$	$-g_{\|\|}^-/2$	0	$g_\perp/2$	0
$\langle^2\Pi_- 1/2\|$	0	$g_{\|\|}^-/2$	0	$g_\perp/2$
$\langle^2\Pi_+ -1/2\|$	$g_\perp/2$	0	$-g_{\|\|}^+/2$	0
$\langle^2\Pi_+ 1/2\|$	0	$g_\perp/2$	0	$g_{\|\|}^+/2$
$L_x + 2S_x$	$\|^2\Pi_- -1/2\rangle$	$\|^2\Pi_- 1/2\rangle$	$\|^2\Pi_+ -1/2\rangle$	$\|^2\Pi_+ 1/2\rangle$
$\langle^2\Pi_- -1/2\|$	0	$g_\perp/2$	0	$-\kappa$
$\langle^2\Pi_- 1/2\|$	$g_\perp/2$	0	κ	0
$\langle^2\Pi_+ -1/2\|$	0	κ	0	$g_\perp/2$
$\langle^2\Pi_+ 1/2\|$	$-\kappa$	0	$g_\perp/2$	0

[a] Parameters are defined by eqs 9, 11, and 12.

$$g_{||}^{\pm} \equiv 2\langle^2\Pi_\pm +1/2|L_z + 2S_z|^2\Pi_\pm +1/2\rangle = 2\,(1 \mp \kappa\Lambda) \quad (11)$$

$$g_\perp \equiv 2\langle^2\Pi_\pm +1/2|L_x + 2S_x|^2\Pi_\pm -1/2\rangle = 2\eta \quad (12)$$

and the components of the angular momentum operators $\boldsymbol{L}$ and $\boldsymbol{S}$ refer to the molecular (x, y, z) reference frame. (We note that $g_x \neq g_y$ in the presence of a CF of Δ symmetry, but the difference, which arises from higher order interactions, is small and unimportant to the following analysis.) These g values are not mutually independent since $\kappa^2 + \eta^2 = 1$ (eqs 8−10); their dependencies on κ are illustrated in Figure 6.

From eq 11 and Figure 6, κ can be seen to act as an orbital reduction factor for the lower ($^2\Pi_-$) SO-CF level. With $\kappa = 1$ (no CF), $g_\perp = 0$, $g_{||}^- = 4$ and the orbital angular momentum makes its full contribution to the magnetic moment. With $\kappa = 0$, the orbital angular momentum is totally quenched, and the g values take their spin-only values.

2. Zeeman Effect. MCD measures the difference between the absorption of left-circularly polarized (lcp) and right-circularly polarized (rcp) radiation propagating along the direction of an externally applied magnetic field (longitudinal Zeeman configuration). Its zeroth moment comprises contributions of two types, referred to as B and C terms:[26]

$$\mathbf{M}_0 = \mathbf{B}_0 + \mathbf{C}_0 \quad (13)$$

C terms, which arise from the first-order Zeeman splittings and the consequent differences between Boltzmann populations of the Zeeman states, are temperature dependent. B terms result from higher order magnetic-field-induced mixing of states and (in the absence of low-lying excited states) are temperature independent.

$\mathbf{C}_0$ is nearly always the dominant contributor to $\mathbf{M}_0$ for paramagnetic systems, and the data in Figures 2−4 clearly show this to be the case for the $A^2\Sigma^+ \leftarrow X^2\Pi$ transition of OH/Ar. In the following, expressions for $\mathbf{C}_0$ are determined explicitly from the first-order Zeeman effect, and then those for $\mathbf{B}_0$ are derived by using perturbation theory. Since the SO-CF splitting of the $X^2\Pi$ term is increased by V (eq 4), we can be certain that $\Delta > 100\ \mathrm{cm}^{-1}$, and at $T < 7$ K the population of the upper SO-CF level can be ignored. Hence only those transitions originating from the $^2\Pi_-$ level are considered.

The nature of the Zeeman effect depends on the angle, θ, that the internuclear axis makes with the magnetic field (Z) axis. The appropriate eigenfunctions and their Zeeman energies are

$$|^2\Pi_- \pm\rangle = a|^2\Pi_- \pm 1/2\rangle \pm b|^2\Pi_- \mp 1/2\rangle \quad (14)$$

$$E_B(\pm) = \pm g_\theta^- \mu_B B/2 \quad (15)$$

where

$$g_\theta^{\pm} = ((g_{||}^{\pm} \cos\theta)^2 + (g_\perp \sin\theta)^2)^{1/2} \quad (16)$$

$$|a|^2 = (g_\perp \sin\theta)^2/(2g_\theta^-\,(g_\theta^- - g_{||}^-\cos\theta)) \quad (17)$$

$$|a|^2 + |b|^2 = 1 \quad (18)$$

$$|a|^2 - |b|^2 = g_{||}^- \cos\theta/g_\theta^- \quad (19)$$

We now define zeroth moments $\mathbf{A}_+$ and $\mathbf{A}_-$, respectively, for the lcp and rcp transitions originating from these eigenstates, utilizing the principle of spectroscopic stability[26] in the choice of excited-state basis functions:

$$\mathbf{A}_\pm = \gamma \sum_{M_\Omega=\pm 1/2} (P_+ |\langle^2\Sigma^+ M_\Omega|\, M_{\pm 1}|^2\Pi_- +\rangle|^2 + P_-\,|\,\langle^2\Sigma^+ M_\Omega|\, M_{\pm 1}|^2\Pi_- -\rangle|^2) \quad (20)$$

γ contains all constant factors, including the concentration and path length of the sample, and $M_{\pm 1} = \mp(2)^{-1/2}(M_X \pm iM_Y)$ are circularly polarized components of the electric dipole operator in a *laboratory-fixed* reference frame where Z designates the direction of the magnetic field. $P_\pm$ are the fractional Boltzmann populations of states $|^2\Pi_- \pm\rangle$:

$$P_\pm = \frac{e^{-E_B(\pm)/kT}}{e^{-E_B(+)/kT} + e^{-E_B(-)/kT}} \quad (21)$$

A and ΔA are, respectively, the average and differential absorbance of circularly polarized radiation. Hence the corresponding zeroth moments are

$$\mathbf{A}_0 = (\mathbf{A}_+ + \mathbf{A}_-)/2 \quad (22)$$

$$\mathbf{C}_0 = \mathbf{A}_+ - \mathbf{A}_- \quad (23)$$

The first step to obtaining more useful expressions for $\mathbf{A}_0$ and $\mathbf{C}_0$ is to relate the matrix elements of $M_{\pm 1}$ to those of the molecule-fixed electric dipole operators, $m_{\pm 1} = \mp(2)^{-1/2}(m_x \pm im_y)$, which are given in Table 3. The resultant terms are then orientationally averaged over Euler angles ψ and ϕ, utilizing the fact that $^2\Sigma^+ \leftarrow {}^2\Pi$ is x, y polarized. The results appropriate to eqs 22 and 23 are

$$|\langle^2\Sigma^+ M_\Omega|M_{+1}|^2\Pi_- \pm\rangle|^2 + |\langle^2\Sigma^+ M_\Omega|M_{-1}|^2\Pi_- \pm\rangle|^2 = ((1+\cos^2\theta)/2)(|\langle^2\Sigma^+ M_\Omega|m_{+1}|^2\Pi_- \pm\rangle|^2 + |\langle^2\Sigma^+ M_\Omega|\, m_{-1}|^2\Pi_- \pm\rangle|^2) \quad (24)$$

TABLE 3: Transition Moments for the $A^2\Sigma^+ \leftarrow X^2\Pi$ SO-CF Transitions of OH/Ar[a]

m_{+1}	$\|^2\Pi_- -\rangle$	$\|^2\Pi_- +\rangle$	$\|^2\Pi_+ -1/2\rangle$	$\|^2\Pi_+ 1/2\rangle$
$\langle^2\Sigma^+ -1/2\|$	$a\alpha M$	$b\alpha M$	$-\beta M$	0
$\langle^2\Sigma^+ 1/2\|$	$-b\beta M$	$a\beta M$	0	$-\alpha M$

m_{-1}	$\|^2\Pi_- -\rangle$	$\|^2\Pi_- +\rangle$	$\|^2\Pi_+ -1/2\rangle$	$\|^2\Pi_+ 1/2\rangle$
$\langle^2\Sigma^+ -1/2\|$	$a\beta M$	$b\beta M$	αM	0
$\langle^2\Sigma^+ 1/2\|$	$-b\alpha M$	$a\alpha M$	0	βM

[a] M is defined by eq 28.

$$|\langle^2\Sigma^+ M_\Omega|M_{+1}|^2\Pi_- \pm\rangle|^2 - |\langle^2\Sigma^+ M_\Omega|M_{-1}|^2\Pi_- \pm\rangle|^2 = \cos\theta(|\langle^2\Sigma^+ M_\Omega|m_{+1}|^2\Pi_- \pm\rangle|^2 - |\langle^2\Sigma^+ M_\Omega|\, m_{-1}|^2\Pi_- \pm\rangle|^2) \quad (25)$$

With Table 3, eqs 8, 9, and 18−25 yield

$$\mathbf{A}_0^\theta = \frac{\gamma\,(1+\cos^2\theta)\,|M\,|^2}{4} \quad (26)$$

$$\mathbf{C}_0^\theta = \frac{\gamma\,\kappa\,g_{||}^{\,-}\cos^2\theta\,|M\,|^2}{g_\theta^{\,-}}\tanh\left(\frac{g_\theta^{\,-}\mu_B B}{2kT}\right) \quad (27)$$

where M is defined in the SO basis;

$$M = \langle^2\Sigma^+ \mp 1/2|m_{\pm 1}|^2\Pi_{3/2}, \mp 3/2\rangle = \mp\langle^2\Sigma^+ \pm 1/2|m_{\pm 1}|^2\Pi_{1/2}, \mp 1/2\rangle \quad (28)$$

Some immediate qualitative conclusions can be drawn from eq 27. First, the existence of a *C* term contribution to the MCD requires $\kappa \neq 0$; that is, the quenching of the orbital angular momentum of OH is incomplete in an Ar host. Second, since all of the parameters are either squared or intrinsically positive, the *C* term contribution to the MCD is positive, as observed experimentally. This result is represented diagrammatically in Figure 5, where the relative intensities of the transitions originating from the $|^2\Pi_- -\rangle$ state are indicated by the thickness of the lines; the total lcp intensity is the greater, so the MCD is positive at low temperatures. Third, the existence of the tanh factor (essentially the population difference $P_- - P_+$) accounts for the saturation behavior exhibited in Figures 3 and 4.

Equations 26 and 27 allow the ratio $\mathbf{C}_0/\mathbf{A}_0$ to be determined for any angle θ. A particularly simple result obtains for the case where $\theta = 0$, whence

$$\mathbf{C}_0^0/\mathbf{A}_0^0 = 2\kappa\tanh\left(\frac{g_{||}^{\,-}\mu_B B}{2kT}\right) \quad (29)$$

However, it is far more likely that the OH molecules are randomly oriented, in which case $\mathbf{A}_0$ and $\mathbf{C}_0$ are obtained by averaging over θ, with the result

$$\mathbf{C}_0/\mathbf{A}_0 = 3\kappa\int_0^1 \frac{g_{||}^{\,-}\cos^2\theta}{g_\theta^{\,-}}\tanh\left(\frac{g_\theta^{\,-}\mu_B B}{2kT}\right)\mathrm{d}\cos\theta \quad (30)$$

The integral in eq 30 cannot be solved analytically, but it does have an approximate solution in the so-called linear limit,[26] where $\mu_B B \ll 2kT$:

$$\mathbf{C}_0/\mathbf{A}_0 \approx \kappa g_{||}^{\,-}\mu_B B/2kT = \kappa(\kappa+1)\mu_B B/kT \qquad (\mu_B B \ll 2kT) \quad (31)$$

Thus the data in Figure 4 show approximately linear behavior in the range $\mu_B B/2kT \lesssim 0.1$. An interesting point to arise from comparison of eqs 30 and 31 is that $g_\perp$ (through its contribution to $g_\theta^{\,-}$; eq 16) is important only outside the linear limit.[29]

We now consider *B*-term contributions to the MCD. The most important of these involves magnetic coupling between $^2\Pi_-$ and $^2\Pi_+$. Invoking spectroscopic stability for the $^2\Pi_+$ states, the appropriate first-order corrections to the $^2\Pi_-$ wave functions are

$$|^2\Pi_- \pm\rangle' = \frac{-\mu_B B}{\Delta}\sum_{M_S=\pm 1/2}|^2\Pi_+ M_S\rangle\langle^2\Pi_+ M_S|L_Z + 2S_Z|^2\Pi_- \pm\rangle \quad (32)$$

where L_Z and S_Z are the projections of the angular momentum operators along the magnetic-field direction. Transforming to the molecular reference frame and keeping only those terms that are of first order in the perturbation yields

$$\mathbf{B}_0^\theta = \gamma(g_\perp\cos\theta)^2\mu_B B|M\,|^2/4\Delta \quad (33)$$

Equation 33 shows that the *B*-term contribution to $\mathbf{M}_0$ does not saturate but (while $\mu_B B \ll \Delta$) increases linearly with the field. When combined with eq 26, the results for the $\theta = 0$ and randomly oriented cases are, respectively

$$\mathbf{B}_0^0/\mathbf{A}_0^0 = g_\perp{}^2\mu_B B/\Delta \quad (34)$$

$$\mathbf{B}_0/\mathbf{A}_0 = g_\perp{}^2\mu_B B/2\Delta \quad (35)$$

3. Data Analysis. The expressions above are functions of only three independent parameters, one of which is the angle θ. The second is the SO coupling constant, for which we choose $\zeta_\pi = 125 \pm 10$ cm^{-1}, slightly less than the gas-phase value.[27,28] The third is chosen to be κ, the orbital reduction factor.

Initially we assume random orientation and vary κ to obtain the best fit to the data of Figure 4 using eqs 13, 30, and 35. We employ standard steepest-descent methods, evaluating the required integrals by Simpson's rule. By choosing κ as the unconstrained parameter, the effects of the uncertainty in ζ_π can be largely restricted to $\mathbf{B}_0$, which is significantly the smaller contribution to $\mathbf{M}_0$. Hence the value of κ is quite insensitive to changes of ζ_π within the estimated range of uncertainty. The best-fit value is $\kappa = 0.79 \pm 0.02$; the *V* and *g* values derived from this result are summarized at the bottom of Table 1.

The best fit, illustrated by the dashed curve in Figure 4, provides an accurate representation of the experimental magnetization behavior. However, it assumes a single effective site for the guest molecules, whereas the structure of the spectra provides evidence that the individual bands represent different sites. First, such an interpretation is consistent with the relative invariance of the structure to isotope and host lattice.[15−17] Second, in the preliminary investigations the relative intensities of the bands showed slight variations with annealing and from one deposition to another. And third, these intensities exhibit different magnetic field and temperature dependencies (Figures 2 and 3), which suggests different κ values.

The last of these points is emphasized in Figure 7, the data for which were obtained by simultaneously fitting the MCD and absorption spectra of Figure 2 with Gaussian bands. These data pertain to temperature dependence within the linear limit; hence eqs 31 and 35 are applicable and *rough* κ values can be estimated from the slopes; these are summarized, along with other parameters derived from them, in Table 1. We emphasize that these values must be treated with caution because of the inherent uncertainties in the fitting procedure in the case of strongly overlapping bands. However, it seems clear that κ does

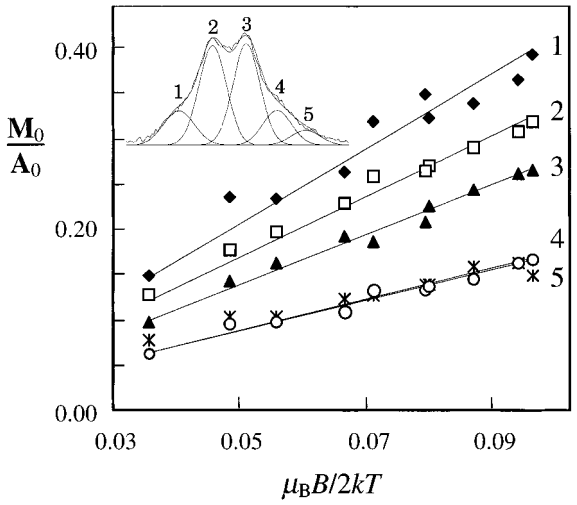

Figure 7. Temperature dependence (at $B = 1$ T) of the ratios $\mathbf{M}_0/\mathbf{A}_0$ for the individual bands (1−5) of Figure 3. The inset illustrates the deconvolution of the 1.73 K MCD spectrum into five Gaussian components. The straight lines are best fits to the temperature-dependence data obtained using eqs 13, 31, and 35. Approximate parameters derived from these fits, assuming random orientation of the guest radical and $\zeta_\pi = 125 \pm 10$ cm^{-1}, are summarized in Table 1.

vary across the envelope of the transition, from higher values at the red end to lower values at the blue.

Finally, we note that evidence has been produced elsewhere to show that larger diatomic molecules (e.g., metal oxides[30−33] and fluorides[34,35]) can assume preferential orientations in rare-gas matrixes, with their internuclear axes either parallel or perpendicular to the plane of the deposition window. For OH/Ar, the former case would eliminate the possibility of observing *C* terms (eq 27) and so can be rejected. For the latter case, eqs 29 and 34 are applicable. Fitting the data of Figure 4 using these expressions yields a substantially smaller orbital reduction factor ($\kappa = 0.48$) but also gives a significantly poorer fit, doubling the sum of the squared residuals. Although we can not definitively exclude the possibility of preferential orientation (with $\theta = 0$), we believe it to be unlikely.

V. Conclusion

The MCD and absorption spectra of OH in Ar confirm a partial quenching of the orbital angular momentum of the lowest electronic level of the guest. A model in which the reduction of angular momentum is due to a low-symmetry crystal field involving neighboring Ar atoms adequately accounts for the observed temperature and magnetic-field dependencies of the MCD. Assuming the radicals to be randomly oriented, the effective average orbital reduction factor is $\kappa = 0.79 \pm 0.02$, corresponding to a crystal field of $V = 97 \pm 10$ cm^{-1}. However, closer consideration of the structure observed in the spectra suggests the guest radicals occupy at least five discrete sites, with orbital reduction factors varying from $\kappa \approx 1$ to 0.5 across the envelope of the transition. In future work we will report matrix-isolation MCD and absorption studies of the NH and CH radicals.

Acknowledgment. We thank Dr. Janna Rose for supplying us with earlier absorption and MCD data for OH/Ar. We are grateful for some helpful comments from one referee. This research was conducted with the aid of funding from the New Zealand Lottery Grant Board, Grant GR 2224987.

References and Notes

(1) Smith, D. *Chem. Rev.* **1992**, *92*, 1473−1485.
(2) Schloerb, F. P.; Claussen, M. J.; Tacconi-Garman, L. *Astron. Astrophys.* **1987**, *187*, 469−474.
(3) Melen, F.; Sauval, A. J.; Grevesse, N.; Farmer, C. B.; Servais, C.; Delbouille, L.; Roland, C. *J. Mol. Spectrosc.* **1995**, *174*, 490−509.
(4) Broida, H. P.; Shuler, K. E. *J. Chem. Phys.* **1952**, *20*, 168−174.
(5) McEwan, M. J.; Phillips, L. F. *Chemistry of the Atmosphere*; Edward Arnold Ltd.: London, 1975.
(6) Halliwell, B.; Gutteridge, J. M. C. *Free Radicals in Biology and Medicine*, 2nd ed.; Oxford University Press: Oxford, 1989.
(7) Halliwell, B.; Gutteridge, J. M. C. *Methods Enzymol.* **1990**, *186*, 1−85.
(8) Watson, W. W. *Astrophys. J.* **1924**, *60*, 145−158.
(9) Mulliken, R. S. *Phys. Rev.* **1928**, *32*, 388−416.
(10) Johnston, H. L.; Dawson, D. H.; Walker, M. K. *Phys. Rev.* **1933**, *43*, 473−480.
(11) Johnston, H. L.; Dawson, D. H. *Phys. Rev.* **1933**, *43*, 580.
(12) Dawson, D. H.; Johnston, H. L. *Phys. Rev.* **1933**, *43*, 980−991.
(13) Huber, K. P.; Herzberg, G. *Molecular Spectra and Molecular Structure*, 1st ed.; Van Nostrand Reinhold: New York, 1979; Vol. 4.
(14) Robinson, G. W.; McCarty, M. J. *J. Chem. Phys.* **1958**, *28*, 350.
(15) Robinson, G. W.; McCarty, M. J. *Can. J. Phys.* **1958**, *36*, 1590−1591.
(16) McCarty, M. J. Ph.D. Dissertation, John Hopkins University, Baltimore, 1960.
(17) Wei, S., unpublished data cited in ref 18.
(18) Tinti, D. S. *J. Chem. Phys.* **1968**, *48*, 1459−1464.
(19) Brus, L. E.; Bondybey, V. E. *J. Chem. Phys.* **1975**, *63*, 786−793.
(20) Rose, J. L. Ph.D. Dissertation, University of Virginia, Charlottesville, 1987.
(21) Piette, L. H.; Rempel, R. C.; Weaver, H. E.; Fluornoy, J. M. *J. Chem. Phys.* **1959**, *30*, 1623−1624.
(22) Siegel, S.; Baum, L.; Skolnik, S.; Fluornoy, J. M. *J. Chem. Phys.* **1960**, *32*, 1623−1624.
(23) Symons, M. C. R. *J. Chem. Soc. London* **1963**, *32*, 570−576.
(24) Brivati, J. A.; Symons, M. C. R.; Tinling, D. J. A.; Wardale, H. A.; Williams, D. O. *Chem. Commun.* **1965**, 402−403.
(25) Dunford, C. L.; Williamson, B. E. *J. Phys. Chem. A* **1997**, *101*, 2050−2054.
(26) Piepho, S. B.; Schatz, P. N. *Group Theory in Spectroscopy with Applications to Magnetic Circular Dichroism*; Wiley-Interscience: New York, 1983.
(27) Samet, C.; Rose, J. L.; Schatz, P. N.; O'Brien, M. C. M. *Chem. Phys. Lett.* **1989**, *159*, 567−572.
(28) Lund, P. A.; Smith, D.; Jacobs, S. M.; Schatz, P. N. *J. Phys. Chem.* **1984**, *88*, 31−42.
(29) Schatz, P. N.; Mowery, R. L.; Krausz, E. R. *Mol. Phys.* **1978**, *35*, 1537−1557.
(30) Kasai, P. H. *J. Chem. Phys.* **1968**, *49*, 4979−4984.
(31) Knight, L. B. J.; Easley, W. C.; Weltner, W. J. *J. Chem. Phys.* **1971**, *54*, 1610−1617.
(32) Knight, L. B. J.; Wise, M. B.; Davidson, E. R.; McMurchie, L. E. *J. Chem. Phys.* **1982**, *76*, 126−136.
(33) Williamson, B. E.; Roser, D. C.; Vala, M. *J. Phys. Chem.* **1994**, *98*, 3624−3630.
(34) Knight, L. B. J.; Easley, W. C.; Weltner, W. J.; Wilson, M. *J. Chem. Phys.* **1971**, *54*, 322−329.
(35) Knight, L. B. J.; Mouchet, A.; Beaudry, W. T.; Duncan, M. *J. Magn. Reson.* **1978**, *32*, 383−390.